Journal of Manufacturing Processes 83 (2022) 105–115

Contents lists available at ScienceDirect

Journal of Manufacturing Processes

journal homepage: www.elsevier.com/locate/manpro

Tempering kinetics during multilayer laser additive manufacturing of a ferritic steel

T. Mukherjee [a], T. DebRoy [a,*], T.J. Lienert [b], S.A. Maloy [c], C.R. Lear [d], P. Hosemann [e]

[a] Department of Materials Science and Engineering, The Pennsylvania State University, University Park, PA 16802, United States of America
[b] Optomec, Inc. Albuquerque, NM 87109, United States of America
[c] Reactor Materials and Mechanical Design, Pacific Northwest National Laboratory, Richland, WA 99354, United States of America
[d] MPA-CINT, Los Alamos National Laboratory, Los Alamos, NM 87545, United States of America
[e] Department of Nuclear Engineering, University of California, Berkeley, CA 94704, United States of America

ARTICLE INFO

Keywords:
3D printing
Directed energy deposition
Martensite
Heat transfer and fluid flow
Neural network
Johnson Mehl Avrami
Grade 91 steel

ABSTRACT

Grade 91 steel forms martensite during additive manufacturing and the extent of tempering of martensite significantly affects the mechanical properties of parts. Currently, there is a lack of quantitative understanding of the tempering kinetics for Grade 91 steel, and as a result, the effects of repeated thermal cycles on properties for different processing conditions cannot be determined. Here we evaluate the tempering kinetics by determining the constant terms in the Johnson Mehl Avrami kinetic equation from the tempering data available in the literature and the thermal cycles computed using a rigorously-tested heat and fluid flow model of multi-layer additive manufacturing. The raw tempering data are cleaned using a neural network to enhance accuracy. The lower layers experience repeating cycles of heating and cooling when the upper layers are added. As a result, the hardness is reduced owing to the tempering of martensite. In contrast, martensite formed in the upper layers is not tempered to the same extent and the hardness remains high. Therefore, the hardness of the part increases with the distance from the substrate. Variations in the heat input at different laser powers and scanning speeds significantly affect the extent of tempering. Since the method used here can provide a quantitative understanding of the tempering of martensite and the spatial variation of hardness, it can be used to tailor the microstructure and hardness of heat treatable printed metallic parts.

1. Introduction

Grade 91 steel, containing 9 % Cr, 1 % Mo, 0.1 % C is a good candidate for structural components in the nuclear energy industry owing to its strength, creep resistance, and high radiation tolerance at service temperature [1,2]. This steel is extensively used in wrought, welded, normalized, and tempered forms [2]. However, the maturity of the technology for the production of components of this steel by additive manufacturing (AM) is at a technological readiness level of 3 (TRL-3) [3]. This low TRL reflects the complexity of tailoring the microstructure and properties that result from the spatially non-uniform temperature fields, rapid cooling, and repeated thermal cycles during AM [4]. For example, rapid cooling during AM results in the formation of martensite that significantly affects the strength, hardness, and toughness of the components [4]. Repeated heating and cooling while depositing multiple layers [5–7] temper the martensite [1] and locally reduce the hardness of the component. The extent of the tempering of martensite and the resulting reduction in hardness are affected by the thermal cycles [8] and thus are influenced by the process parameters such as laser power, scanning speed, layer thickness, laser spot size, and preheat temperature [9]. Understanding the roles of the process parameters on the tempering of martensite and the spatial variation in hardness are important since they significantly influence the quality of the printed parts and their serviceability in industrial applications.

Several kinetic models [10–12] were developed to explain the tempering kinetics by capturing the formation of martensite and tempered martensite. For example, Johnson Mehl Avrami (JMA) equation-based model was implemented to capture the mechanisms of tempering of martensite during welding of a martensitic steel [13]. Tempering kinetics were also modeled for multi-pass fusion welding of a commonly used ferritic-martensitic steel to show the variations in martensite fraction after each welding pass [14]. In AM, JMA equation-

* Corresponding author.
E-mail address: debroy@psu.edu (T. DebRoy).

https://doi.org/10.1016/j.jmapro.2022.08.061
Received 20 May 2022; Received in revised form 23 August 2022; Accepted 30 August 2022
Available online 6 September 2022

Table 1
Properties of Grade 91 steel used in the modeling. These properties represent the thermo-physical behavior of the alloy and affect the thermal cycles. Here, thermal conductivity and specific heat are taken as temperature dependent and the temperature in K is represented by 'T'. The properties were calculated using the commercial software, JMatPro.

Properties	Values
Liquidus temperature (K)	1775
Solidus temperature (K)	1690
Thermal conductivity (W/m K)	$16.63 + 1.02 \times 10^{-2}$ T
Specific heat (J/ kg K)	$250.0 + 0.70$ T $- 2.0 \times 10^{-4}$ T^2
Density (kg/m^3)	7300
Latent heat of fusion (J/kg)	260×10^3
Viscosity (kg/m s)	7×10^{-3}
Temperature coefficient of surface tension, dγ/dT (N/m K)	-0.40×10^{-3}
Thermal conductivity of liquid (W/m K)	32.2
Specific heat of liquid (J/kg K)	824.2

based kinetic models were also used to explain the tempering kinetics [15]. However, the application of these kinetics models is often hindered due to the lack of a sufficient volume of high-quality, reliable tempering data from which the constants of the JMA equation are calculated [8]. This is because the tempering experiments are time-consuming and experiments at different temperatures and tempering times are needed to generate a sufficient volume of data. An alternate solution is to train a neural network [16–18] using the available tempering data and use it to generate a large volume of high-quality data that are subsequently used to calculate the JMA constants. Similar approaches have been used to generate high-quality data for a wide variety of engineering applications, including the boiling point and enthalpy of vaporization for several elements [19], atmospheric temperature [20], and highway asphalt pavement inspection [21].

The JMA equation-based kinetic models capture the tempering kinetics based on experimentally measured thermal cycles. However, measurement of thermal cycles is not possible at every location in a component [5]. Rapid movement of a very small molten pool during AM also makes the measurement of temperature challenging [5]. A recourse is to calculate the thermal cycles using well-tested mechanistic models [22] of the AM process and use the computed thermal cycles in a kinetic model to evaluate the tempering kinetics. These mechanistic models solve the equations of conservation of mass, energy, and momentum [23–25] by discretizing them in a computational domain. Depending on the size of the computational domain, often billions of equations are solved iteratively in a computationally efficient way. For example, to simulate a track of 10 mm length we need about 250,000 control volumes and 1000 time steps. If we solve for 5 variables (temperature, pressure, and three components of velocity) with 100 iterations for each time step to achieve a good convergence we need to solve (250,000 × 1000 × 5 × 100) 125 billion equations.

Here we combined a rigorously-tested, transient, three-dimensional heat transfer and fluid flow model [23,24] and a JMA equation-based model [26] to evaluate the tempering kinetics of martensite during laser directed energy deposition (DED-L) of Grade 91 steel used in nuclear energy applications. Accurate thermal cycles were computed using the heat and fluid flow model at various places in the part for different process parameters. The thermophysical properties of the Grade 91 steel (Table 1) needed in the model were estimated by performing thermodynamic calculations using a commercial package, JMatPro [27]. The alloy-specific constants in the JMA kinetic model were computed using high-quality tempering data obtained from a neural network [16–18]. The neural network was trained using available tempering data for Grade 91 steel from the literature [28] and was used to generate a large volume of high-quality tempering data for various combinations of temperature and tempering time. The JMA equation was then integrated by cumulatively adding small isothermal time steps over a computed thermal cycle to evaluate the extent of tempering. The analysis using the heat transfer and fluid flow model, JMA kinetic model, neural network-based machine learning, and tempering data provided a quantitative framework to evaluate the kinetics of tempering of martensite during multi-layer printing that was not possible to obtain in any other way. The methodology was also used to evaluate the influence of power and speed of the laser beam on the tempering kinetics.

2. Methodology

The methodology used here is schematically shown in Fig. 1. First, a neural network [16–18] was trained using tempering data on Grade 91 steel collected from the literature [28]. Then the trained neural network was used to generate high-quality tempering data for various combinations of temperature and tempering time. The constants in the JMA equation were calculated using the tempering data obtained from the neural network. A rigorously-validated, transient, three-dimensional heat and fluid flow model [23,24] of directed energy deposition - laser (DED-L) was utilized to compute thermal cycles at various places in the part. Then the JMA equation was integrated by cumulatively adding small isothermal time steps over a computed thermal cycle to estimate the hardness. Because the hardness variation in a component is directly related to the fraction of a phase changed to another phase [29–31], the extent of tempering was computed from the calculated values of the hardness. The assumptions made in the calculations are discussed below.

2.1. Assumptions

The following simplifying assumptions were made for the heat transfer and fluid flow model and the JMA equation-based calculations:

(i) Fluid flow inside the molten pool is Newtonian and incompressible.
(ii) The turbulence in the fluid flow was considered by using uniform enhancement of thermal conductivity and viscosity [23].
(iii) Recoil pressure on the molten pool surface due to vaporization was ignored. This assumption was made because the molten pool surface temperature was significantly below the boiling point of the alloy.
(iv) Liquid material properties were considered to be independent of temperature.
(v) Fluid flow in the two-phase mushy zone was modeled following the Carmen-Kozeny equation for fluid flow through a porous medium [23].
(vi) The JMA equation obtained from tempering data was used for the tempering kinetics in additive manufacturing. Since the kinetic data during AM are not available, this assumption provides a tractable framework for quantitative understanding of kinetics that cannot be obtained otherwise. This approach has proved to be of value in previous independent research. For example, JMA constants using conventional heat treatment data for H13 tool steel were successfully used [33] to model the kinetics during DED-L of H13 tool steel.
(vii) The JMA relation was established using the aging data for Grade 91 steel. The computed hardness was tested with the available data for Grade 92 steel since no data for Grade 91 were available. Since the chemical compositions of these two steels differ in Mo and W concentrations as shown in Table 2, the errors in the predictions of the hardness were evaluated and reported in Section 3.

2.2. Generation of high-quality tempering data using a neural network

A neural network was used to generate high-quality tempering data for various combinations of tempering time and temperature. The

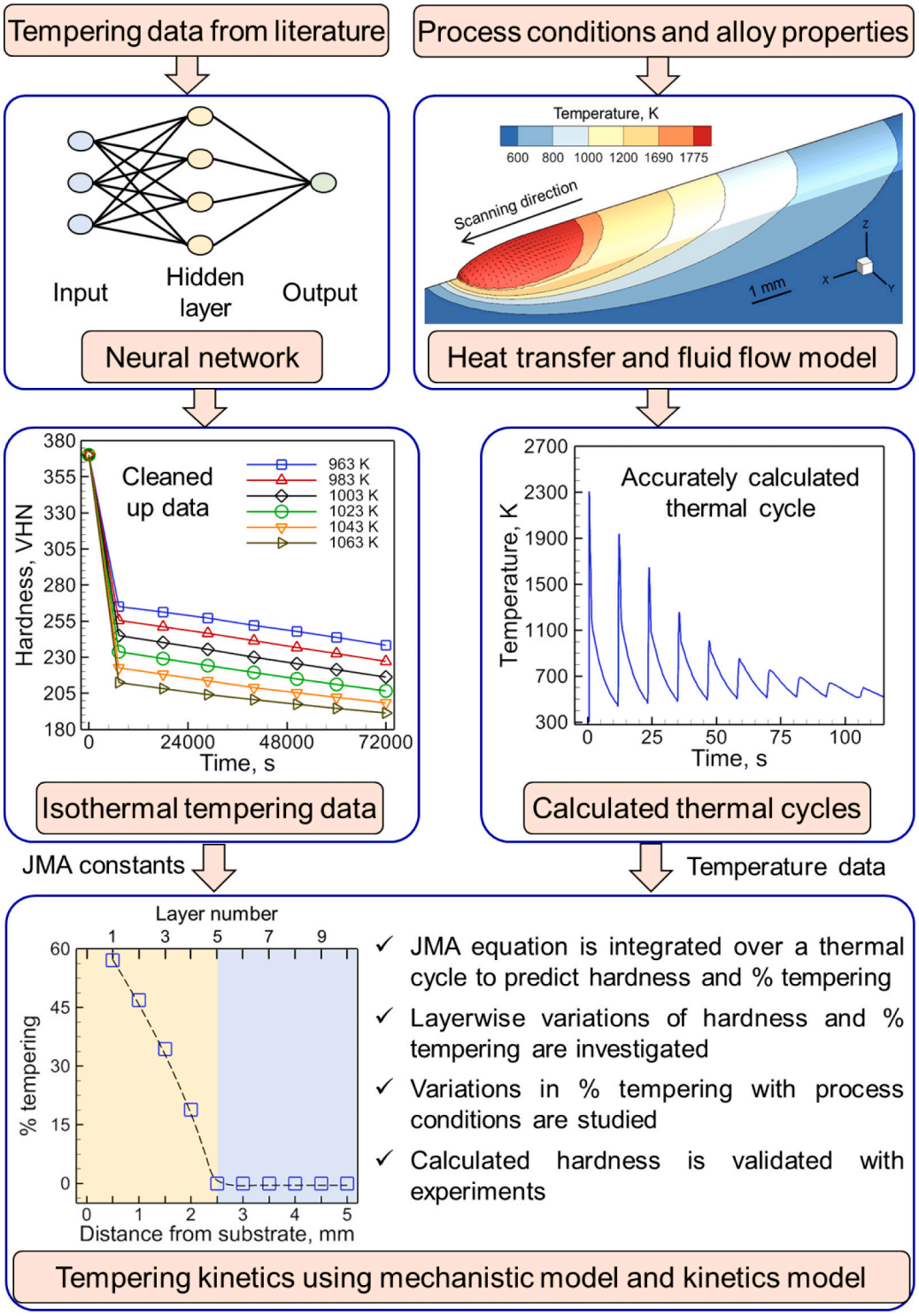

Fig. 1. Schematic representation of the methodology used here. Here we used a heat transfer and fluid flow model, JMA kinetic model, neural network-based machine learning, and tempering data to provide a framework for evaluating the kinetics of tempering of martensite during multi-layer printing.

relation between the hardness and aging time and temperature is not known. Since the neural network does not require any explicit relation between the variables, it is the best choice in this case. The neural network was trained using tempering data of Grade 91 steel reported by Shrestha, et al. [28]. The data are tabulated in the Supplementary Document. The data contains measured hardness values of Grade 91 steel for different initial hardness values, tempering temperatures, and tempering times. These three parameters serve as inputs to the neural network, with one output, hardness after tempering. In the neural network, a hyperbolic tangent function was fit using all training data by implementing an error back-propagation algorithm [16–18] that minimizes the logarithmic error to update the weights linking different hidden layers. The number of hidden layer and hidden nodes were taken as one and six, respectively. The neural network calculations were done using a well-tested in-house code [17] compiled in the Intel Fortran Compiler. The details of the neural network are explained in Appendix

Table 2
Chemical compositions (in wt%) of ASTM A387 Grade 91 steel and ASTM A335 Grade 92 steel.

Elements	Grade 91	Grade 92
Cr	7.90–9.60	8.50–9.50
Mo	0.80–1.10	0.30–0.60
V	0.16–0.27	0.15–0.25
Nb	≤ 0.08	0.04–0.09
Mn	0.25–0.66	0.30–0.60
Cu	≤ 0.18	–
Ni	≤ 0.43	≤ 0.40
Ti	≤ 0.01	–
Al	≤ 0.02	≤ 0.40
Zr	≤ 0.01	–
C	0.06–0.15	0.07–0.13
Si	0.18–0.56	≤ 0.50
P	≤ 0.025	≤ 0.020
S	≤ 0.012	≤ 0.010
N	0.025–0.080	0.030–0.070
W	–	1.50–2.00
B	–	0.001–0.006
Fe	Balance	Balance

[Note: Grade 91 composition is available at: www.alloysteelplates.com/astm-a387-grade-91-class-1.html.
Grade 92 composition is available at: www.metalspiping.com/astm-a335-p92.html].

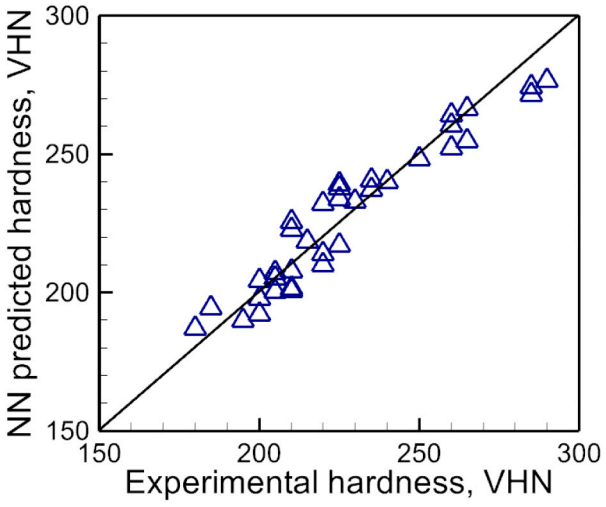

Fig. 2. A plot showing the hardness predicted by a neural network (NN) versus the experimentally measured hardness [28] values that were used to train the neural network. There are 36 data points taken from the literature for Grade 91 steel. The data are tabulated in the Supplementary Document. The mean absolute error in training the neural network is 6.8 VHN.

A. Fig. 2 shows a plot of hardness predicted by the trained neural network versus the experimentally measured hardness values that were used to train the neural network. The proximity of the data points to the diagonal line (mean absolute error = 6.8 VHN) indicates that the neural network is well-trained.

The trained neural network was used to generate tempering data for different tempering times and temperatures. Fig. 3 provides the tempering data output by the neural network. The data shows the variation in the hardness values with the tempering time at various temperatures. During tempering, the hardness of Grade 91 steel parts decreases as the martensite changes to tempered martensite, forming chromium and vanadium carbides (Fig. 3). Because tempering is thermally activated, an increase in tempering temperature leads to a greater reduction in hardness (Fig. 3). These tempering data were used to calculate JMA equation constants as described below.

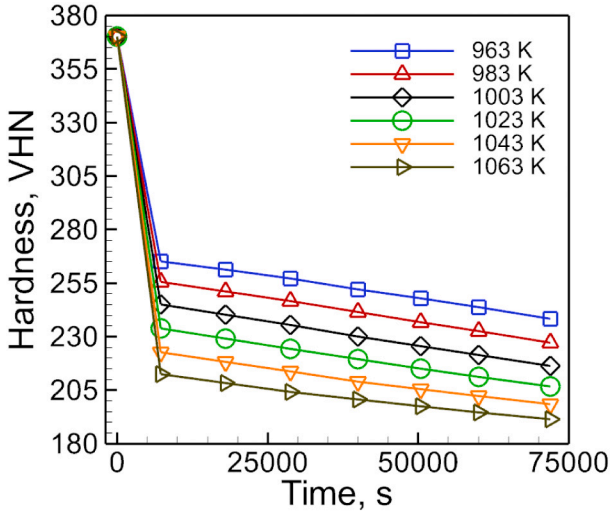

Fig. 3. Tempering data for Grade 91 steel showing the hardness at different temperatures and tempering times. These data are obtained from a neural network. The initial hardness is 370 VHN. The data are tabulated in the Supplementary Document.

2.3. Calculations of constant terms in the Johnson Mehl Avrami (JMA) equation

The constants in the JMA kinetic equation were computed using the tempering data of Grade 91 steel obtained from the neural network. The hardness variation in a component is directly related to the fraction of a phase changed to another phase [29–31]. Therefore, the extent of tempering (Y) can be expressed as a function of change in hardness (H) as,

$$Y = \frac{H_0 - H}{H_0 - H_\infty} \tag{1}$$

where H_0 is the initial hardness which was taken as 370 VHN which was the maximum hardness value (Fig. 3). H_∞ indicates the hardness of a part after very long tempering and its value was taken as 184 VHN. H denotes the hardness of a part whose values at different times and temperatures were taken from the tempering diagram (Fig. 3). Variations in the extent of tempering with the tempering time for various temperatures are represented in Fig. 4 (a).

From the JMA equation, the extent of tempering (Y) is expressed as [32],

$$Y = 1 - exp[-\mathrm{k}(t)^n] \tag{2}$$

where t is time in seconds and n and k indicate the constant terms in the JMA equation. Therefore, the magnitudes of ln(k) and n (Table 3) can be found at different temperatures from the Y-intercepts and slopes of Fig. 4 (b), respectively. In addition, k is expressed as [32],

$$k = k_0 exp(-Q/RT) \tag{3}$$

where k_0 is a constant that depends on the material used, Q denotes the activation energy needed for the transformation in J/mol K, T indicates the temperature in K, and R represents the universal gas constant whose value is 8.314 J/mol K. The value of Q/R was estimated from the slope of the ln(k) versus $1/T$ plot (Fig. 5), where Q = 3.01×10^4 J/mol. In addition, the Y-intercept of the same plot indicated the value of $\ln(k_0) = 2.0$ which gave $k_0 = 7.31$ (seconds)$^{-0.19}$. A mean value of n for different temperatures (Table 3) was calculated as n = 0.19 and was used in the calculation.

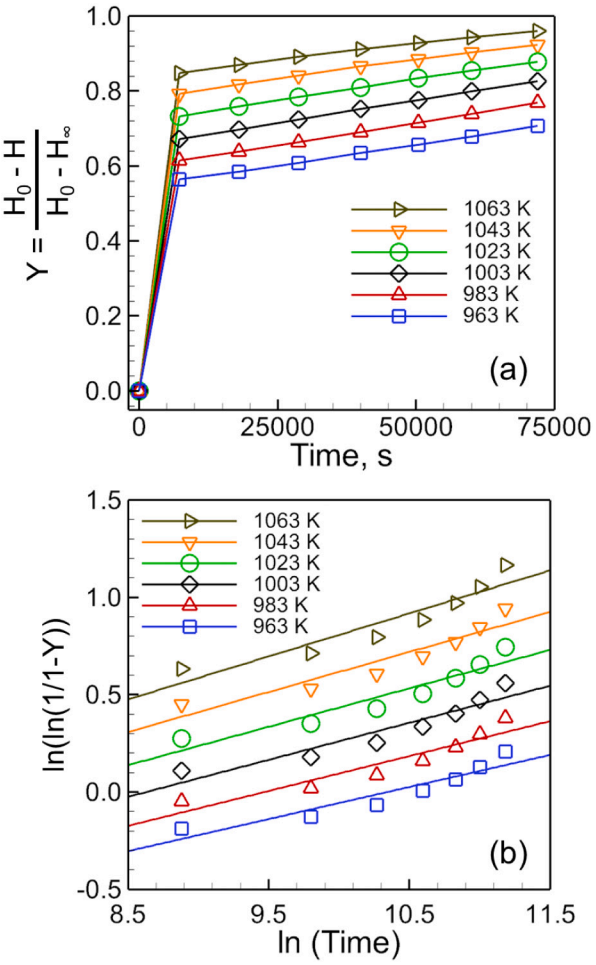

Fig. 4. Plots needed to predict the JMA constants for Grade 91 steel. (a) Variations in the quantity Y (extent of tempering) with respect to tempering time for various tempering temperatures. Here, 'H' represents the Vicker's hardness in Fig. 3. H_0 and H_∞ have their values as 370 and 184 VHN, respectively. (b) Plot for extracting the magnitudes of the variable, ln(k) and n. 'Y' values are taken from figure (a). The magnitudes of the variables, ln(k) and n can be extracted from the y-intercepts and slopes of different lines and are supplied in Table 3. 'k' has a unit of $(seconds)^{-0.19}$. Since the JMA equation is plotted in logarithmic scale in figure (b), the initial phase of the plot appears to be nearly linear with a relatively larger separation among two consecutive data points.

Table 3
The values of ln(k) and n at different temperatures needed to calculate the constants used in the JMA equation. These two variables are calculated using isothermal tempering data of Grade 91 steel. The slopes and y-intercepts of the lines in Fig. 4 (b) provide n and ln(k), respectively.

Temperature, K	ln (k)	n
963	−1.72	0.16
983	−1.70	0.18
1003	−1.64	0.19
1023	−1.54	0.20
1043	−1.44	0.21
1063	−1.40	0.22
Average n		0.19

2.4. Calculation of thermal cycles using the heat and fluid flow model

A well-tested, 3D, transient heat transfer and fluid flow model [23,24] was used to calculate the thermal cycles during DED-L. The model solved the equations of conservation of energy, mass, and momentum to compute the 3D temperature and velocity distributions. Multiple thermal cycles at various places in the part were extracted from the computed temperature field. The model was discussed in detail and rigorously tested in our previous publications [23,24] and is not discussed here again. The important features in applying the well-tested model are described below.

Calculations were performed using the cartesian coordinate for multi-layer thin walls. For all layers, a unidirectional scanning of the laser beam was used along the positive X-axis. The direction of building multiple layers was taken along the positive *Z*-axis. The positive Y-axis was perpendicular to the direction of the laser scanning and represented the direction along the width of the deposit. Half of the computational domain was used in the calculations by assuming symmetry on both sides of the vertical XZ plane. This assumption was made to make the model computationally efficient. The model was developed using an in-house Fortran code compiled in an Intel Compiler. The thermophysical properties of the Grade 91steel needed in the model were estimated using a commercial package JMatPro [27] and are presented in Table 1.

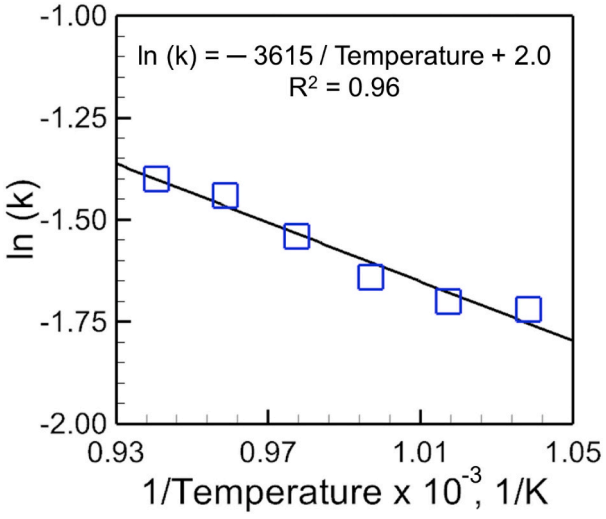

Fig. 5. A linear plot between ln(k) given in Table 3 and 1/temperature. The value of Q/R was estimated from the slope of the plot, where $Q = 3.01 \times 10^4$ J/mol. In addition, the value of y-intercept of the plot indicated the magnitude of $\ln(k_0) = 2.0$ which gave $k_0 = 7.31$ $(seconds)^{-0.19}$. The R^2 value of 0.96 indicates a good linear fitting of the data.

2.5. Prediction of the extent of tempering and hardness

The extent of tempering of martensite and the resulting change in hardness are affected by the thermal cycle. It was assumed that a thermal cycle is a cumulative addition of many very small time steps (Δt) at constant temperatures (T). The addition of these small isothermal time steps (Δt) over the complete thermal cycle included the entire tempering process [33],

$$\sum \frac{\Delta t}{t} = 1 \tag{4}$$

where t represents time in seconds and Δt is in seconds. The time (t) indicated the time needed to reach a given value of hardness (H) at a particular temperature (T) according to the isothermal JMA equation. Therefore, the value t can be estimated by combining Eqs. (1)–(3) as,

$$t = \left[\frac{ln\left(1 - \frac{H_0 - H}{H_0 - H_\infty}\right)}{-k_0 exp\left(\frac{-Q}{RT}\right)} \right]^{1/n} \tag{5}$$

where T indicates the temperature in K. Other parameters are explained

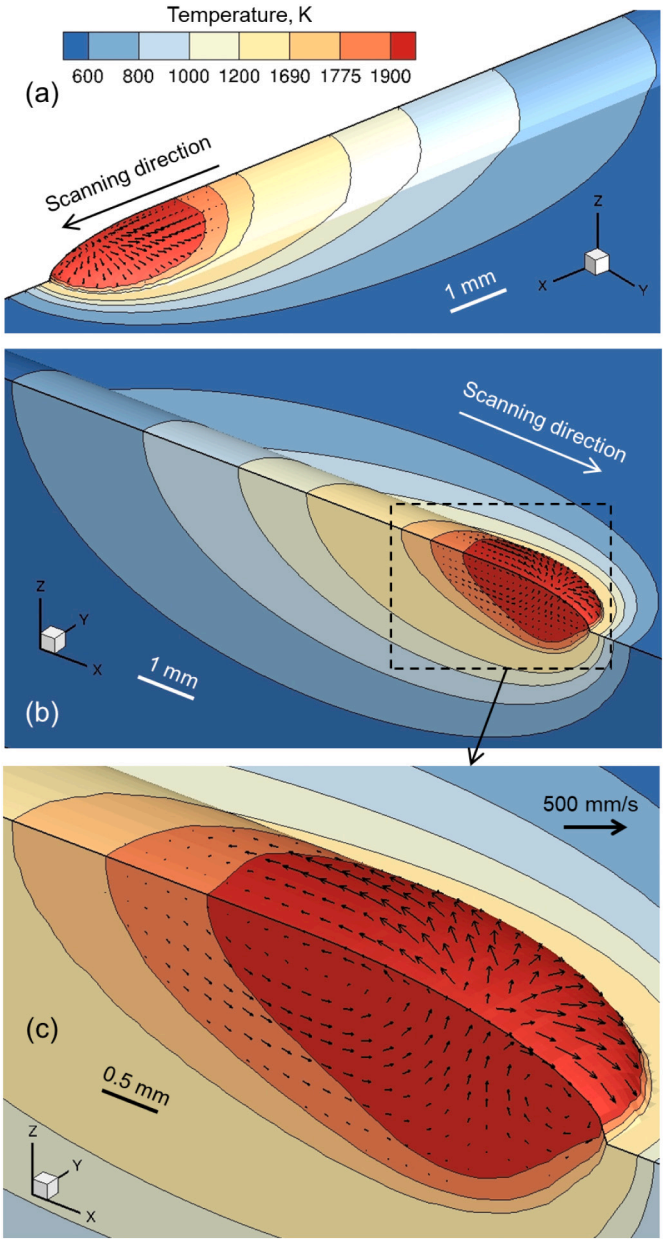

Fig. 6. Temperature and convective velocity distributions in three different 3D isometric orientations (a) and (b). These computed results are for Grade 91 steel processed using DED-L at 800 W power and 6.0 mm/s speed. In addition, other DED-L process variables are supplied in Table 4. Here, half of the computational domain is represented in this figure by taking the advantage of the symmetry with XZ plane. Figure (c) shows a closer view of figure (b) to show the velocity vectors inside the molten pool.

in Section 2.2.

The hardness attained after the part experiences an entire thermal cycle was estimated by using Eq. (4) over a thermal cycle. To do so, the time (t) in Eq. (5) was substituted in Eq. (4) and the time step (Δt) and the temperature (T) were taken from the thermal cycle. Therefore, the only unknown variable is the hardness (H). Then Eq. (4) was solved using many iterations over a computed thermal cycle to calculate the hardness (H) until the condition in that equation is satisfied. Smaller time steps (Δt) provided more accurate results. The extent of tempering (Y) was estimated from the computed hardness by using Eq. (1).

Table 4
Additive manufacturing process variables used in this research.

Process parameters	Values
Laser power (W)	650, 800, 950
Laser scanning speed (mm/s)	4, 6, 8
Laser beam radius (mm)	1.5
Layer thickness (mm)	0.50
Mass feed rate of powders (g/s)	0.133
Substrate thickness (mm)	20

3. Results and discussion

The tempering kinetics of martensite during multi-layer printing of Grade 91 steel is affected by the thermal cycles that are controlled by the 3D, transient temperature field. Fig. 6 shows the 3D temperature and velocity distributions during the deposition of a single-layer Grade 91 steel deposit using DED-L for the processing conditions in Table 4 when the position of the beam was at the half-length of the deposited track. In the figure, the fusion zone is represented by the red area surrounded by the liquidus isotherm (1775 K) of Grade 91 steel. The area between the solidus (1690 K) and liquidus (1775 K) isotherms indicate the two-phase mushy region. Near the front of the molten pool, isotherms are compressed. However, due to the high scanning speed along the positive x-direction, isotherms are elongated near the trailing edge. The deposit exhibits a curved top surface formed due to the accumulation of powders. The deposit height is the maximum at the center of the fusion zone and it decreases with the distance from the center. Black vectors represent the velocity of the flow of the molten material. This convective flow is primarily driven by the spatial gradient of surface tension on the molten pool top surface. In addition, the absolute magnitude of the velocity vectors can be predicted by comparing the length of these vectors with the length of the reference vector given in the figure. The flow of the liquid metal occurs along the curved top surface of the molten pool from the mid-location where surface tension is low to the boundary where the surface tension is high.

Thermal cycles at different places in the part can be estimated from transient, three-dimensional temperature fields (Fig. 6), and hardness can be computed at that location based on the thermal cycle using Eq. (4). Fig. 7 (a) shows that the computed hardness variation along the deposit height for a 10 layers high thin wall agrees well with the corresponding experimental results [34]. These results are for DED-L of Grade 92 steel which has a similar chemical composition and precipitation kinetics as Grade 91 steel. The hardness was measured using a Vickers diamond indenter at multiple heights of the wall [34]. Hardness was calculated using Eq. (4) at the same places where experimental measurements were performed by extracting the thermal cycles at the corresponding locations. It should be noted that the hardness increases with layers until it reaches a critical layer, layer 5, beyond which it remains almost constant. These variations in hardness are explained using the numerically calculated thermal cycles at different layers (Fig. 7 (b–d)), as discussed below.

While depositing a layer, rapid cooling results in the formation of martensite. While depositing the subsequent layers, the martensite suffers from repeated heating and cooling resulting in its phase transformation. If the peak temperature of a deposited layer while depositing subsequent layers exceeds the Ac1 temperature (1123K) [34], the martensite transforms back to the austenite. The austenite upon cooling forms martensite again which affects the local hardness. In contrast, when the peak temperature of a deposited layer while depositing the subsequent layers does not exceed the Ac1 temperature, subsequent heating and cooling transform the martensite into tempered martensite. For the upper layers, for example, the 8th layer (Fig. 7 (d)), the peak temperature always exceeded the Ac1 temperature (1123 K). Therefore, the hardness of those later layers was almost unchanged because the martensite was untempered after re-austenization. However, for the

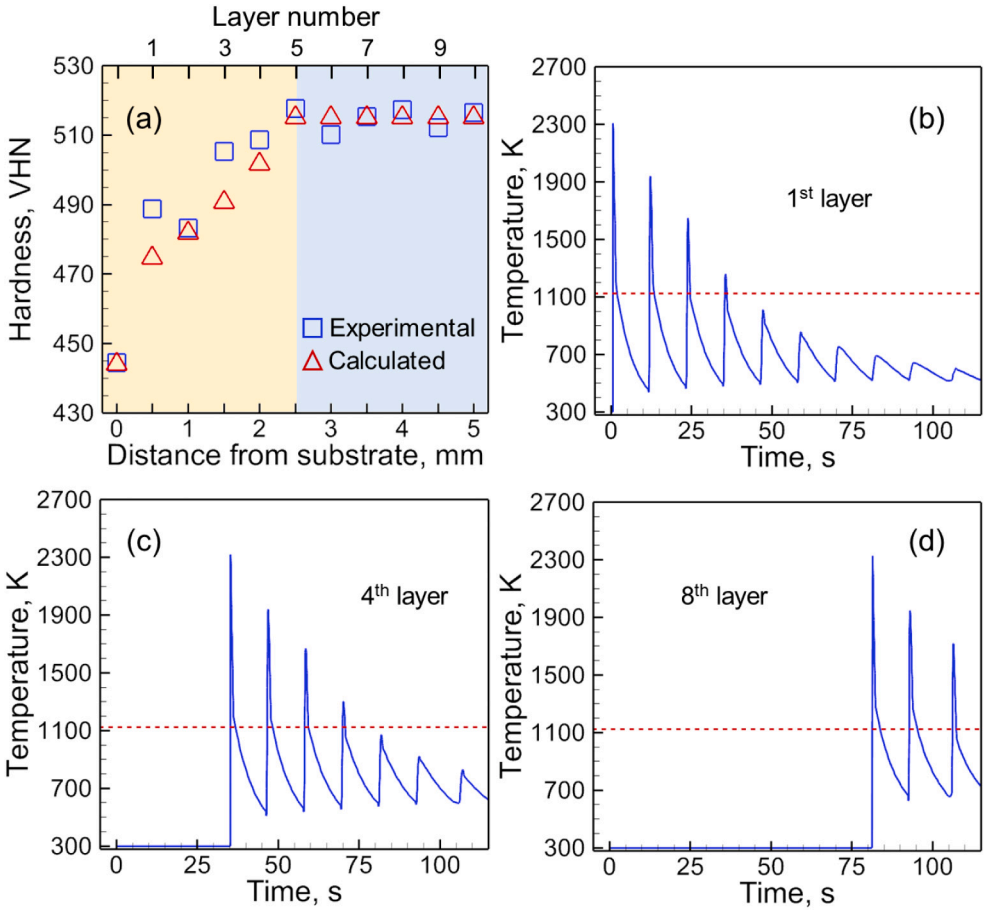

Fig. 7. (a) A plot comparing the computed hardness (in VHN) with the experimentally measured [34] values for Grade 92 steel. The variations in hardness are taken with the distance vertically away from the substrate. These results are simulated along a 10 layers thin wall processed using DED-L at 800 W power and 6.0 mm/s speed. In addition, other DED-L process variables are supplied in Table 4. The root mean square error in hardness prediction in figure (a) is 6.8 VHN. Thermal cycles monitored at the half-length, mid-width of the track on the top surface of the (b) 1st, (c) 4th, and (d) 8th layer while depositing the 10 layers. The temperature corresponding to the horizontal red dashed line indicates the Ac1 temperature (1123 K). (For interpretation of the references to colour in this figure legend, the reader is referred to the web version of this article.)

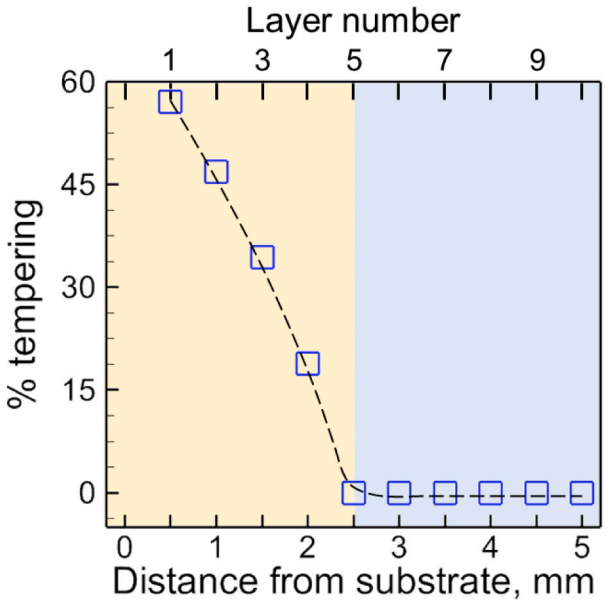

Fig. 8. Variations in the extent of tempering (computed using eq. (1)) of martensite with the distance from the substrate during DED-L of a Grade 91 thin-wall (10 layers tall) using 800 W power and 6.0 mm/s speed. In addition, other DED-L process variables are listed in Table 4.

lower layers, for example, the 1st and 4th layers (Fig. 7 (b, c)), the peak temperature did not exceed the Ac1 temperature after the deposition of a few subsequent layers. The repeating cycles of heating and cooling below the Ac1 temperature gradually transformed the martensite to the tempered martensite and reduced the hardness proportionally. For example, the 1st layer (Fig. 7 (b)) experienced more thermal cycles than the 4th layer (Fig. 7 (c)) and exhibited lower hardness. In short, with the deposition of layers, the extent of tempering decreased (Fig. 8) and the hardness increased (Fig. 7 (a)) until a critical layer was reached beyond which the hardness remained unchanged.

Figs. 7 and 8 show that variations in the extent of tempering and the resulting hardness are strongly influenced by the local thermal cycles and thus by process parameters such as the power and speed of the laser beam. Two opposing factors contribute to these variations, (i) the number of thermal cycles below Ac1 temperature and (ii) the temperatures sustained during these cycles. High power or slow scanning speed indicates a high heat input that results in a high temperature. Under such conditions, a layer experiences fewer thermal cycles below Ac1 temperature (1123 K) resulting in a less amount of martensite transformed into tempered martensite. In contrast, more tempering can take place due to a high temperature at high power and slow scanning speed. Figs. 9 and 10 provide examples to explain the effects of power and speed of the laser beam, respectively, on the layer-wise variations in the extent of tempering, as discussed below.

We consider the 1st and 3rd layers as examples. The 3rd layer experienced three, two, and one thermal cycles below Ac1 temperature (1123 K) at 650 W, 800 W, and 950 W laser powers, respectively (Fig. 9 (a)). Therefore, the 3rd layer exhibited the maximum percentage of tempering at 650 W (Fig. 9 (b)) because it experienced the highest numbers of thermal cycles below Ac1 temperature. Similarly, the 1st layer experienced five, four, and three thermal cycles below Ac1 temperature at 650 W, 800 W, and 950 W laser powers, respectively (Fig. 9 (a)). Therefore, the 1st layer experienced the minimum percentage of tempering at 950 W because it experienced the least number of thermal

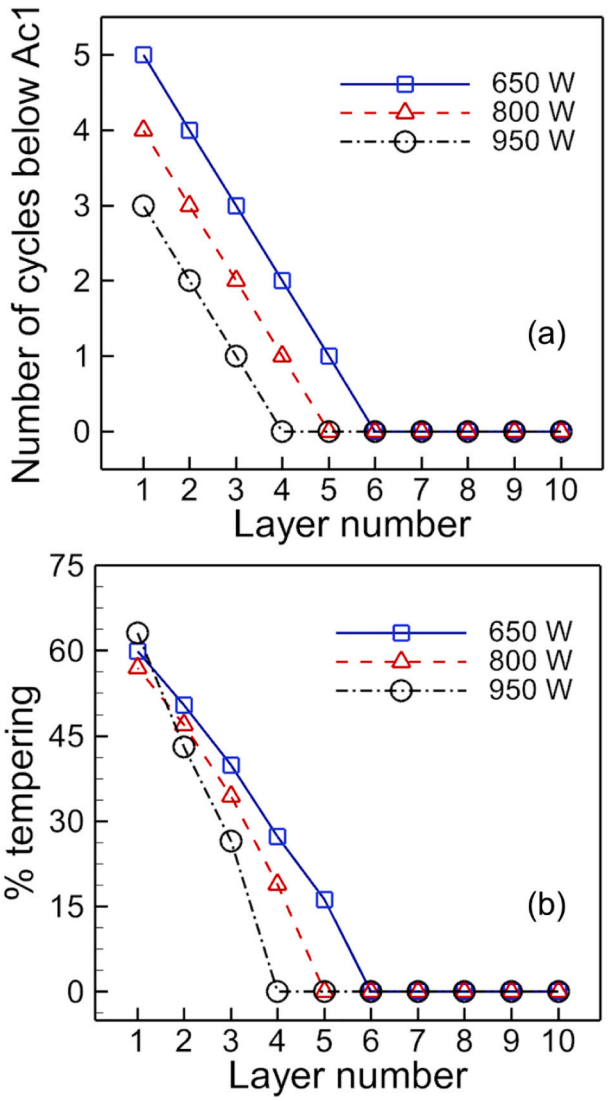

Fig. 9. (a) Number of thermal cycles below Ac1 and (b) computed variations in the percentage of tempering of martensite with layer number during DED-L of a Grade 91 thin wall (10 layers tall) at different laser powers and at a constant scanning speed of 6 mm/s. In addition, other DED-L process variables are listed in Table 4.

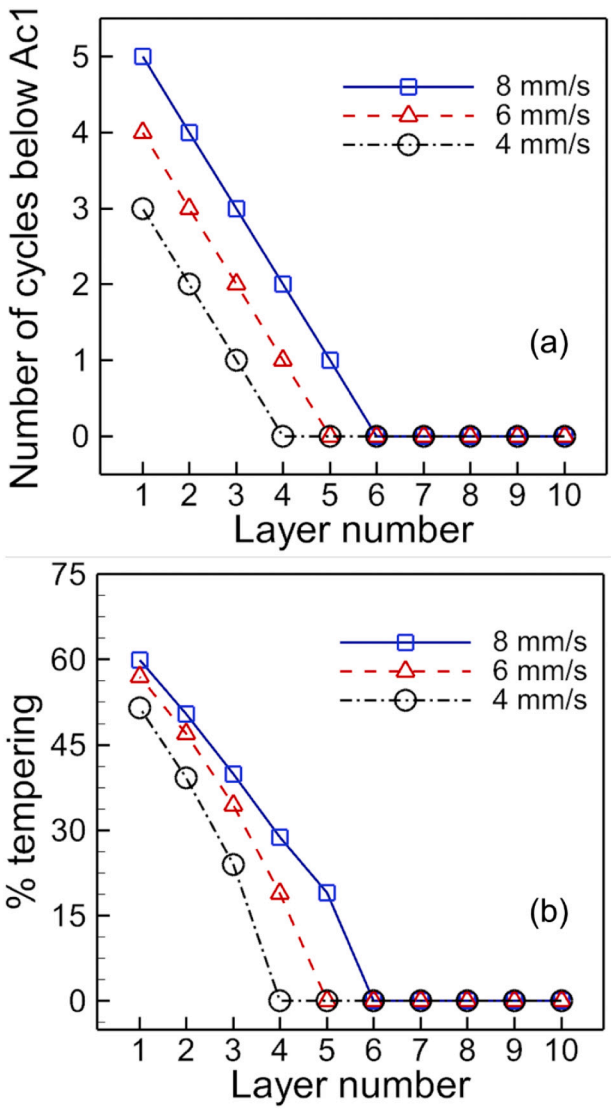

Fig. 10. (a) Number of thermal cycles below Ac1 and (b) computed variations in the percentage of tempering of martensite with layer number during DED-L of a Grade 91 thin wall (10 layers tall) at different scanning speeds and at a constant power of 800 W. In addition, other DED-L process variables are listed in Table 4.

cycles below Ac1 temperature. However, the 1st layer also experienced the highest temperature at 950 W which transformed more martensite into tempered martensite. The percentage of tempering at the 1st layer was decided by these two opposing factors. Consequently, the extent of tempering at the first layer was the highest at 950 W (Fig. 9 (b)) where the second factor was more influential than the first one. Therefore, for different layers, the effect of laser power on the extent of tempering varied significantly depending on the number of thermal cycles below Ac1 temperature and the peak temperature. Similar observations were made in Fig. 10 where significant variations in the extent of tempering were observed at various layers at three different scanning speeds. Therefore, the extent of tempering of martensite and the resulting hardness of the part can be controlled by adjusting the heat input by altering the laser power and scanning speed. However, care should be taken while adjusting the heat input so that it does not form defects such as cracking, lack of fusion voids, distortion [35,36].

Since the method used here can provide a quantitative understanding of the tempering of martensite and the variation in hardness, it can be used to tailor the microstructure and hardness of some printed metallic parts of heat-treatable alloys. The methodology of combining mechanistic model, machine learning, JMA kinetic model, and experimental data can also be used to evaluate the phase transformation kinetics in other engineering alloys. Examples may include the kinetics of the formation of precipitates in the precipitation-hardened nickel and aluminum alloys. However, it needs high-quality and reliable tempering data for those alloys and well-tested thermophysical properties of alloys to compute the thermal cycles, and thus requires significant research efforts in this area.

4. Summary and conclusions

In summary, we evaluated the tempering kinetics of Grade 91 steel during multi-layer additive manufacturing using the Johnson Mehl Avrami kinetic relation and thermal cycles computed by a heat transfer and fluid flow model. The parameters of the JMA kinetic relation were derived based on tempering data obtained from the literature and cleaned using a neural network. The computed results show fair agreement with the experiments. Below are the important findings:

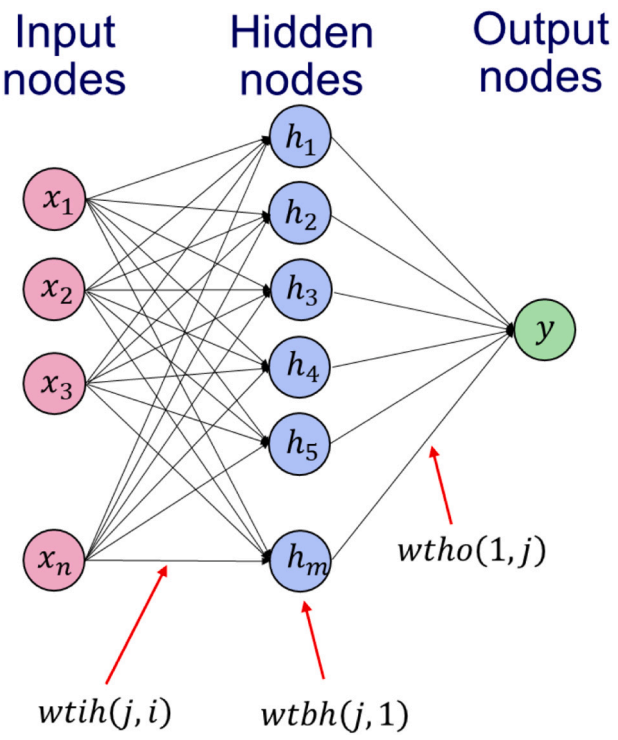

Fig. 11. The basic structure of a neural network [17].

1) The initially deposited layers of a multi-layer deposit experienced repeated thermal cycles that tempered the martensite and thus reduced hardness. In contrast, the martensite in the upper layers was not tempered and retained its high hardness. Therefore, the hardness of the part increases with the distance from the substrate and the extent of tempering of the martensite follows the opposite trend. However, the hardness variation depends on the specimen size and the nature of variation may be different for taller specimens.
2) The extent of tempering at different heat inputs resulted from two opposing factors: (i) the number of thermal cycles below Ac1 temperature and (ii) the peak temperatures attained during these cycles. High heat input at high power or slow speed of the laser beam resulted in a high temperature. Under such conditions, a layer experienced fewer thermal cycles below Ac1 temperature (1123 K) resulting in a less extensive tempering of martensite and relatively higher hardness. In contrast, more martensite was transformed to tempered martensite at a high temperature caused by high heat input.
3) During multilayer additive manufacturing, there is a critical height of the deposit above which the hardness and extent of tempering remained almost unchanged. For the layers above the critical height, the peak temperature exceeded the Ac1 temperature (1123 K) and the martensite was transformed to austenite. The austenite upon cooling formed martensite again. Therefore, the hardness for those layers was affected by the amount of martensite and remained almost unchanged. High heat input owing to the slow speed or high power of the laser beam moved the critical deposit height close to the substrate.

Declaration of competing interest

The authors declare that they have no known competing financial interests or personal relationships that could have appeared to influence the work reported in this paper.

Acknowledgments

This work was supported by the funding received from the DOE Office of Nuclear Energy's Nuclear Energy Enabling Technologies Program, as part of project 19–17206 of the Advanced Methods for Manufacturing Program.

Data availability statement

The raw/processed data required to reproduce these findings cannot be shared at this time due to technical or time limitations.

Appendix A. Working principle of the neural network

First, a neural network was trained using the aging data from the literature that had a lot of fluctuations and the volume of available data was not sufficient to reliably estimate the JMA parameters. The trained network was used to generate a sufficient volume of high-quality data that was used to estimate the JMA parameters. In the neural network, all training data were used to fit a hyperbolic tangent function by using an error back-propagation algorithm [16–18] that minimizes the logarithmic error to update the weights linking different hidden layers. The number of hidden layers and hidden nodes were taken as one and six, respectively. There are three inputs and one output. The output was computed with the following hyperbolic tangent function:

$$\mathrm{y} = tanh\left(\sum_{i=1}^{n} w_i \mathrm{x_i} + \theta_i\right) \tag{6}$$

where x_i and y are the input and the output of a hidden node, w_i is the weight, n is the total number of inputs ($n = 3$) and θ_i is the bias dependent on the ith input. The neural network model with the least log predictive error was selected as the best model and used for the validation and testing data sets. For a better understanding of the neural network, the basic structure of the NN is shown in Fig. 11. The number of input nodes is $i = 1, n$, and the number of hidden nodes is $j = 1, m$. Here, the values of n and m are 3 and 6, respectively. The weight matrix from input nodes to hidden nodes is $wtih(j, i)$, and the bias coefficient for each hidden node is $wtbh(j, 1)$, and the weight matrix from hidden nodes to output nodes is $wtho(1, j)$.

For our case, feeding the neural network with three input variables, the best number of hidden nodes is 6 and the corresponding weight matrix for $wtih(j, i)$, $wtbh(j, 1)$ and $wtho(1, j)$ are provided below.

$$\mathrm{wtih(i,j)} = \begin{bmatrix} -0.25 & -0.13 & 0.027 \\ -0.266 & -0.139 & 0.028 \\ -0.266 & -0.139 & 0.028 \\ -0.266 & -0.139 & 0.028 \\ 0.265 & 0.138 & -0.028 \\ -0.266 & -0.139 & 0.028 \end{bmatrix}$$

$$\text{wtbh}(j,1) = \begin{bmatrix} 0.297 \\ 0.317 \\ 0.317 \\ 0.317 \\ -0.316 \\ 0.317 \end{bmatrix} \quad \text{wtho}(1j)\text{T} = \begin{bmatrix} -0.075 \\ -0.081 \\ -0.081 \\ -0.081 \\ 0.080 \\ -0.081 \end{bmatrix}$$

Appendix B. Supplementary data

Supplementary data to this article can be found online at https://doi.org/10.1016/j.jmapro.2022.08.061.

References

[1] Lienert TJ, Maloy SA. Laser additive manufacturing of F/M steels for radiation tolerant nuclear components, no. LA-UR-17-30052. Los Alamos, NM: Los Alamos National Lab; 2017. https://doi.org/10.2172/1407859.

[2] David SA, Siefert JA, Feng Z. Welding and weldability of candidate ferritic alloys for future advanced ultrasupercritical fossil power plants. Sci Technol Weld Join 2013;18(8):631–51. https://doi.org/10.1179/1362171813Y.0000000152.

[3] Balbaud F, Cabet C, Cornet S, Dai Y, Gan J, Mayoral MH, et al. A NEA review on innovative structural materials solutions, including advanced manufacturing processes for nuclear applications based on technology readiness assessment. Nucl Mater Energy 2021;27:101006. https://doi.org/10.1016/j.nme.2021.101006.

[4] Eftink BP, Vega DA, El Atwani O, Sprouster DJ, Yoo YSJ, Steckley TE, et al. Tensile properties and microstructure of additively manufactured grade 91 steel for nuclear applications. J Nucl Mater 2021;544:152723. https://doi.org/10.1016/j.jnucmat.2020.152723.

[5] DebRoy T, Wei HL, Zuback JS, Mukherjee T, Elmer JW, Milewski JO, et al. Additive manufacturing of metallic components - process, structure and properties. Prog. Mater. Sci. 2018;92:112–224. https://doi.org/10.1016/j.pmatsci.2017.10.001.

[6] DebRoy T, Mukherjee T, Wei HL, Elmer JW, Milewski JO. Metallurgy, mechanistic models and machine learning in metal printing. Nat Rev Mater 2021;6(1):48–68. https://doi.org/10.1038/s41578-020-00236-1.

[7] DebRoy T, Mukherjee T, Milewski JO, Elmer JW, Ribic B, Blecher JJ, et al. Scientific, technological and economic issues in metal printing and their solutions. NatMater 2019;18:1026–32. https://doi.org/10.1038/s41563-019-0408-2.

[8] Mukherjee T, DebRoy T, Lienert TJ, Maloy SA, Hosemann P. Spatial and temporal variation of hardness of a printed steel part. Acta Mater 2021;209:116775. https://doi.org/10.1016/j.actamat.2021.116775.

[9] Manvatkar V, De A, DebRoy T. Spatial variation of melt pool geometry, peak temperature and solidification parameters during laser assisted additive manufacturing process. Mater Sci Technol 2015;31:924–30. https://doi.org/10.1179/1743284714Y.0000000701.

[10] Wu YX, Sun WW, Gao X, Styles MJ, Arlazarov A, Hutchinson CR. The effect of alloying elements on cementite coarsening during martensite tempering. Acta Mater 2020;183:418–37. https://doi.org/10.1016/j.actamat.2019.11.040.

[11] Galindo-Nava EI, Rivera-Díaz-del-Castillo PEJ. A model for the microstructure behaviour and strength evolution in lath martensite. Acta Mater 2015;98:81–93. https://doi.org/10.1016/j.actamat.2015.07.018.

[12] Malheiros LRC, Rodriguez EAP, Arlazarov A. Mechanical behavior of tempered martensite: characterization and modeling. Mater Sci Eng A 2017;706:38–47. https://doi.org/10.1016/j.msea.2017.08.089.

[13] Biro E, McDermid JR, Vignier S, Zhou YN. Decoupling of the softening processes during rapid tempering of a martensitic steel. Mater Sci Eng A 2014;615:395–404. https://doi.org/10.1016/j.msea.2014.07.102.

[14] Sun YL, Obasi G, Hamelin CJ, Vasileiou AN, Flint TF, Francis JA, Smith MC. Characterisation and modelling of tempering during multi-pass welding. J Mater Process Technol 2019;270:118–31. https://doi.org/10.1016/j.jmatprotec.2019.02.015.

[15] Zhang Q, Xie J, Gao Z, London T, Griffiths D, Oancea V. A metallurgical phase transformation framework applied to SLM additive manufacturing processes. Mater Des 2019;166:107618. https://doi.org/10.1016/j.matdes.2019.107618.

[16] Jordan MI, Mitchell TM. Machine learning: trends, perspectives, and prospects. Science 2015;349(6245):255–60. https://doi.org/10.1126/science.aaa8415.

[17] Du Y, Mukherjee T, Mitra P, DebRoy T. Machine learning based hierarchy of causative variables for tool failure in friction stir welding. Acta Mater 2020;192:67–77. https://doi.org/10.1016/j.actamat.2020.03.047.

[18] LeCun Y, Bengio Y, Hinton G. Deep learning. Nature 2015;521(7553):436–44. https://doi.org/10.1038/nature14539.

[19] Zhang Y, Evans JRG, Yang S. Corrected values for boiling points and enthalpies of vaporization of elements in handbooks. J Chem Eng Data 2011;56(2):328–37. https://doi.org/10.1021/je1011086.

[20] Owolabi O, Okoh D, Rabiu B, Obafaye A, Dauda K. A median absolute deviation-neural network (MAD-NN) method for atmospheric temperature data cleaning. MethodsX 2021;8:101533. https://doi.org/10.1016/j.mex.2021.101533.

[21] Han C, Zhang W, Ma T. Data cleaning framework for highway asphalt pavement inspection data based on artificial neural networks. Int. J Pavement Eng. 2021:1–13. https://doi.org/10.1080/10298436.2021.2001813.

[22] Wei HL, Mukherjee T, Zhang W, Zuback JS, Knapp GL, De A, DebRoy T. Mechanistic models for additive manufacturing of metallic components. Prog Mater Sci 2021;116:100703. https://doi.org/10.1016/j.pmatsci.2020.100703.

[23] Knapp GL, Mukherjee T, Zuback JS, Wei HL, Palmer TA, De A, DebRoy T. Building blocks for a digital twin of additive manufacturing. Acta Mater 2017;135:390–9. https://doi.org/10.1016/j.actamat.2017.06.039.

[24] Wei HL, Knapp GL, Mukherjee T, DebRoy T. Three-dimensional grain growth during multi-layer printing of a nickel-based alloy Inconel 718. Addit Manuf 2019;25:448–59. https://doi.org/10.1016/j.addma.2018.11.028.

[25] Ou W, Knapp GL, Mukherjee T, Wei Y, DebRoy T. An improved heat transfer and fluid flow model of wire-arc additive manufacturing. Int J Heat Mass Trans 2021;167:120835. https://doi.org/10.1016/j.ijheatmasstransfer.2020.120835.

[26] Málek J, Mitsuhashi T. Testing method for the Johnson–Mehl–Avrami equation in kinetic analysis of crystallization processes. J Am Ceram Soc 2000;83(8):2103–5. https://doi.org/10.1111/j.1151-2916.2000.tb01523.x.

[27] Saunders N, Guo UKZ, Li X, Miodownik AP, Schillé J. Using JMatPro to model materials properties and behavior. JOM 2003;55(12):60–5. https://doi.org/10.1007/s11837-003-0013-2.

[28] Shrestha T, Alsagabi SF, Charit I, Potirniche GP, Glazoff MV. Effect of heat treatment on microstructure and hardness of grade 91 steel. Metals 2015;5(1):131–49. https://doi.org/10.3390/met5010131.

[29] Pogatscher S, Antrekowitsch H, Leitner H, Ebner T, Uggowitzer PJ. Mechanisms controlling the artificial aging of Al-Mg-Si alloys. Acta Mater 2011;59:3352–63. https://doi.org/10.1016/j.actamat.2011.02.010.

[30] Esmaeili S, Lloyd DJ, Poole WJ. Modeling of precipitation hardening for the naturally aged Al-Mg-Si-Cu alloy AA6111. Acta Mater 2003;51:3467–81. https://doi.org/10.1016/S1359-6454(03)00167-8.

[31] Sekhar AP, Nandy S, Ray KK, Das D. Prediction of aging kinetics and yield strength of 6063 alloy. J Mater Eng Perform 2019;28(5):2764–78. https://doi.org/10.1007/s11665-019-04086-z.

[32] Crespo A, Vilar R. Finite element analysis of the rapid manufacturing of Ti–6Al–4V parts by laser powder deposition. Scr Mater 2010;63(1):140–3. https://doi.org/10.1016/j.scriptamat.2010.03.036.

[33] Brooks J, Robino C, Headley T, Goods S, Griffith M. Microstructure and property optimization of LENS deposited H13 tool steel. Int. Solid Freeform Fab. Symp. 1999. https://doi.org/10.26153/tsw/830.

[34] Xia Z, Xu J, Shi J, Shi T, Sun C, Qiu D. Microstructure evolution and mechanical properties of reduced activation steel manufactured through laser directed energy deposition. Addit Manuf 2020;33:101114. https://doi.org/10.1016/j.addma.2020.101114.

[35] Oliveira JP, Santos TG, Miranda RM. Revisiting fundamental welding concepts to improve additive manufacturing: from theory to practice. Prog Mater Sci 2020;107:100590. https://doi.org/10.1016/j.pmatsci.2019.100590.

[36] Mukherjee T, DebRoy T. Printability of 316 stainless steel. Sci Technol Weld Join 2019;24(5):412–9. https://doi.org/10.1080/13621718.2019.1607061.

T. Mukherjee, Dr. Mukherjee is a Postdoctoral Researcher at the Pennsylvania State University where he earned his Ph.D. in Materials Science and Engineering. His research interests include additive manufacturing, welding, machine learning, multi-physics modeling, heat and mass transfer, thermal distortion, and residual stress. He has published several papers in leading international journals including Nature Reviews Materials, Nature Materials, and Progress in Materials Science. He has recently edited a book entitled "The Science and Technology of 3D Printing" and served as a Guest Editor for the journals "Computational Materials Science", "Materials", and "Science and Technology of Welding and Joining".

T. DebRoy, Dr. DebRoy is a Professor of Materials Science and Engineering at Penn State and the author of 370 papers, 5 edited books, and a 2021 book on "Innovations in Everyday Engineering Materials." He has served as a Fulbright Distinguished Chair in Brazil, Distinguished Visiting Professor at IIT Bombay, Aditya Birla Chair at IISc, Bangalore, UK Royal Academy of Engineering Distinguished Visiting Fellow at Cambridge University, and Visiting Professor at KTH, Stockholm. He is a Founding Editor of the journal "Science and Technology of Welding and Joining."

T.J. Lienert, Dr. Lienert is Senior LENS Scientist, Optomec, Owner, TJ Lienert Consulting, LLC, and a former President of the American Welding Society (AWS). He was formerly a technical staff member and an R&D engineer 4 at Los Alamos National Laboratory for >16 years. He has published many peer-reviewed papers on additive manufacturing, welding, and materials science and several book and handbook chapters. He is a Fellow of the American Welding Society and ASM International.

S.A. Maloy, Dr. Maloy is a Senior Nuclear Materials Advisor for Reactor Materials and Mechanical Design at The Pacific Northwest National Laboratory (PNNL). A registered

professional engineer (PE) in Metallurgy, he previously worked for Los Alamos National Laboratory for 33 years and is a National Laboratory Professor at the University of New Mexico. His research focuses on the behavior of materials in extreme environments such as under neutron and proton irradiation at reactor-relevant temperatures. He is the author of >250 peer-reviewed technical papers.

C.R. Lear, Dr. Lear is a Research Associate at the Los Alamos National Laboratory (LANL). He earned his Ph.D. from The University of Illinois at Urbana-Champaign and was a Postdoctoral Researcher at the University of Michigan, Ann Arbor. His research focuses on the behavior of materials in extreme environments and advanced characterization of alloys and he is the author of many papers in these areas.

P. Hosemann, Dr. Hosemann is a Professor in the Department for Nuclear Engineering at the University of California, Berkeley, and the current department chair, head graduate adviser, and UC Berkeley's radiation safety chair. His research features experimental material science for extreme environments, especially nuclear environments. His focus is on structural materials used for nuclear components while developing a basic understanding of the materials degradation processes and resulting consequences to engineering applications. He has authored >140 peer-reviewed papers and won the TMS Early-career Faculty Fellow award and the AIME Robert Lansing Hardy award.